Three-dimensional simulation of shoaling internal solitary waves and their influence on particle transport in the southern Red Sea

Item Type	Article
Authors	Guo, Daquan;Zhan, Peng;Hoteit, Ibrahim
Citation	Guo, D., Zhan, P., & Hoteit, I. (2021). Three-dimensional simulation of shoaling internal solitary waves and their influence on particle transport in the southern Red Sea. Journal of Geophysical Research: Oceans. doi:10.1029/2020jc016335
Eprint version	Post-print
DOI	10.1029/2020jc016335
Publisher	American Geophysical Union (AGU)
Journal	Journal of Geophysical Research: Oceans
Rights	Archived with thanks to Journal of Geophysical Research: Oceans
Download date	2024-03-13 09:08:38
Link to Item	http://hdl.handle.net/10754/668225

Three-dimensional simulation of shoaling internal solitary waves and their influence on particle transport in the southern Red Sea

Daquan Guo[1], Peng Zhan[1], Ibrahim Hoteit[1]

[1]King Abdullah University of Science and Technology, Thuwal, 23955-6900

Key Points:

- First 3D high-resolution realistic simulation of ISW shoaling process in the southern Red Sea
- Simulation results indicate that the ISW shoaling process in the southern Red Sea follows a mild breaking process
- Particle transport are examined quantitatively, showing significant influence of the ISW shoaling process on the particles movements

Corresponding author: Ibrahim Hoteit, `Ibrahim.hoteit@kaust.edu.sa`

–1–

Abstract

The shoaling process of a group of internal solitary waves (ISWs) in the southern Red Sea is simulated with a 3D, non-hydrostatic, high-resolution MIT general circulation model (MITgcm). The breaking and dissipation processes are well reproduced, in which a positive tail forms behind and locally moves the interface upward, causing the transformation of wave polarity as it moves onshore. With the step-like structure followed, the wave eventually evolve into smaller water bores. Combined with the parameters of the leading wave slope (S_w) of about 0.07 and topography slope (S) of about 0.01, the shoaling is suggested to follow a mild breaking process.

The particle transport during the shoaling process is further examined quantitatively using the Connectivity modelling system (CMS). 38400 particles are released at six different vertical layers in the main shoaling domain. Most of the particles are transported up-and-down following the wave oscillation process then settle within 10-20 m around the original released depth. For the particles inside the breaking area, the oscillation process becomes more complex and intensified, and eventually a great portion of these particles settle far away from their released locations. The time-integrated transport distance, T_i, and the direct transport distance, T_s, are also analyzed. With T_i almost 20 times to T_s in vertical, continuous up-and-down movements are suggested during the shoaling process.

Plain Language Summary

Internal solitary waves (ISWs), generated and propagates inside the ocean, bring significant mixing when they comes to the shore interacting with the topography, which is important for both physical and biological ocean systems. In this study, we simulate the shoaling process of a group of internal solitary waves in the southern Red Sea and the particle transport during this process. A careful examination of certain parameters suggests the breaking mechanism of ISWs in the southern Red Sea to follows a mild breaking process. The particle transport is examined quantitatively with 38400 particles released at six different vertical layers in the main shoaling domain. Both vertical and horizontal movements under the influence of the shoaling ISWs are tracked and analyzed. The integrated transport distance Ti and the distance between that at the beginning and the last snapshot Ts are also analyzed. With Ti almost 20 times to Ts in vertical, continuous up-and-down movements are suggested during the shoaling process.

1 Introduction

Internal waves are ubiquitous in the world ocean, especially in marginal seas and shelves [*Simmons et al.*, 2004; *Garrett and Kunze*, 2007]. Internal solitary waves (ISWs), one type of internal waves, commonly evolve from the baroclinic tides due to non-linearity effects and usually feature relative large wave amplitude from ten to one hundred meters [*Guo*, 2013]. Because of their large amplitudes, ISWs contribute to the seawater property exchange and may have a significant influence on the physical, chemical and biological systems [*Alford et al.*, 2015]. One of the most important processes during the life-long period of ISWs is the shoaling processes, during which the energetic ISWs propagate into the shallow area and interact with the bottom topography, eventually breaking and dissipating into small scale process under the strong nonlinear effects and bottom friction. Observations have shown that the shoaling process of internal waves could affect the transport of physically and biologically important scalars such as temperature [*Leichter et al.*, 1996; *Davis and Monismith*, 2011; *Walter et al.*, 2012], nutrients [*Leichter et al.*, 1996; *Omand et al.*, 2011], sediments [*Bogucki et al.*, 1997; *Klymak and Moum*, 2003; *Hosegood et al.*, 2004; *Carter et al.*, 2005; *Quaresma et al.*, 2007; *Droghei et al.*, 2016], larvae [*Pineda*, 1994, 1995, 1999] and dissolved oxygen [*Walter et al.*, 2014].

The complexity of the shoaling process and difficulty for capturing them with in-situ observations make the laboratory experiments and numerical simulations better approaches for the study of this process. A number of previous studies have been conducted, with various focuses on the kinematics of wave breaking [*Wallace and Wilkinson*, 1988; *Helfrich and Pineda*, 2003; *Vlasenko and Hutter*, 2002; *Venayagamoorthy and Fringer*, 2007; *Sutherland et al.*, 2013], classifying breaker types [*Boegman et al.*, 2005; *Aghsaee et al.*, 2010; *La Forgia et al.*, 2018a], wave reflection [*Bourgault and Kelley*, 2007; *Aghsaee et al.*, 2010] and quantifying turbulence and mixing [*Michallet and Ivey*, 1999; *Boegman et al.*, 2005; *Arthur and Fringer*, 2014; *Venayagamoorthy and Fringer*, 2006, 2007; *La Forgia et al.*, 2018b, 2020]. *Pineda* [1994] suggested that internal tidal bores produce upwelling by advecting subsurface water to the near shore and play a key role in the exchange across the shelf of material and water properties. Specifically, the advection of masses of water by internal bores transports onshore larvae near the thermocline or living close to the sea-floor [*Pineda*, 1995; *Leichter et al.*, 2003]. The deep cold water pushes the warm water offshore, creating a front that can be found up to at least 2 km from the shore; as the cold water sinks, the front dividing cold and warm water concentrates and

transports neustonic larvae [*Pineda*, 1994, 1999]. *Pineda* [1999] concluded that the internal tidal-bore phenomena explains well the transport of both water column and neustonic larvae in different habitats. *Scotti et al.* [2008] studied the shoaling process of nonlinear internal waves in the Massachusetts Bay using a fully nonlinear and nonhydrostatic model, showing that the process is dominated by nonlinearity. They further investigated the results of a two-layer, nonlinear, but hydrostatic model. *Aghsaee et al.* [2010] classified the breaker types into surging, plunging and collapsing, depending on their reflection, convective instability and boundary-layer separation. The breaker types is characterized in wave slope versus space, and the reflection coefficient, modelled as a function of the internal Iribarren number, in agreement with previous studies [*Boegman et al.*, 2005]. More recently, *Arthur and Fringer* [2016] studied the transport by breaking internal gravity waves, based on the results of numerical simulations with a particle-tracking model, using idealized bottom slopes. Onshore and offshore transport together with their mechanisms were studied and sensitivity experiments focusing on the initial wave amplitudes were investigated and discussed *Arthur and Fringer* [2016].

Recently, ISWs have been observed by satellite images along the off-shelf region of the southern Red Sea between 16.0 °N and 16.5 °N [*Da Silva et al.*, 2012]. Using 2D numerical simulations, *Guo et al.* [2016] revealed that the generation process follows a standard nonlinear evolution process of an internal tide. These ISWs mostly dissipates after propagating into the slopes and interacting with the bottom topography, before reaching the continental shelves near the islands, as suggested by the satellite observations [*Da Silva et al.*, 2012] and numerical simulations [*Guo et al.*, 2016]. The ecosystem around Farasan islands is ecologically significant and hosts some of the most diverse corals species in the Red Sea [*Gladstone*, 1996; *Riegl et al.*, 2012]. Annual aggregations of parrot-fish occur in the region of Farasan islands, where the 'Hareed Festival' fishing event is held every year [*Gladstone*, 1996; *Berumen et al.*, 2013]. As the shoaling process of ISWs enforces significant vertical movements and mixing of seawater, influences on the nutrients and larvae at this particular region are expected, which makes it a favorable laboratory for studying the particle transport during the shoaling process of ISWs.

In this study, we employ a non-hydrostatic high-resolution MIT general circulation model (MITgcm) to simulate the full shoaling process of ISWs in the southern Red Sea with realistic topography and ocean conditions. Based on the outputs of the model, we then simulate the particle transport during the shoaling process using a particle-tracking

111 model, the Connecting Modeling System (CMS), and reveal that significant vertical and

112 horizontal transports of particles during the shoaling process of ISWs. To the best of our

113 knowledge, this is the first study that investigates particle transport of a realistic case

114 of ISW shoaling process. The rest of the paper is organized as follows. Section 2 describes

115 the methodology, including the model configuration of MITgcm and CMS. The simu-

116 lations results of the shoaling process of ISWs are presented and discussed in Section 3.

117 The analysis of the particle transport with the ISWs is described in Section 4. Section

118 5 summarizes the main results of this study and discusses their significance and impli-

119 cations on the future research.

2 Methodology

121 Two numerical models are employed in this study. The state-of-the-art MITgcm

122 is implemented to simulate the shoaling process of the ISWs in the southern Red Sea,

123 and the CMS is implemented to explore the particles transport during the shoaling pro-

124 cess. The configurations of the two models are presented below.

2.1 Non-hydrostatic MITgcm ocean model

126 Version c65x of MITgcm is implemented to simulate the 3D ISW shoaling process.

127 The present configuration of MITgcm employs the nonhydrostatic version of the finite-

128 volume, incompressible Navier-stokes equations, designed to study oceanic phenomena

129 at both large- and small-scales [*Marshall et al.*, 1997]. The equations and their imple-

130 mentation are detailed in https://doi.org/10.5281/zenodo.1409237. The model domain

131 is shown in Figure 2. The bottom topography is derived from ETOPO-1. To damp the

132 topography influence to the initial-balance process of the ISWs, the west slope is removed

133 and the maximum depth is set to 1200 m. The pathway of the shoaling process includes

134 both headlands and banks, providing appropriate conditions for exploring the 3D dy-

135 namics of the process. The model is configured on a grid of horizontal resolution 75 m

136 with 1680 ×1440 grid points. Vertically, 170 layers are implemented with 1 m resolution

137 at the surface and exponentially to 10 m at the mid-depth, and with uniform 10 m lay-

138 ers from mid-depth to bottom. Sponge zones are implemented at the last 50 grid points

139 of all four open boundaries, increasing exponentially from 75 m to 6562 m, to absorb the

140 wave energy and avoid reflecting. Following *Guo et al.* [2016], temperature and salinity

141 fields are derived from the World Ocean Atlas (WOA) 2005 and interpolated homoge-

–5–

¹⁴² neously in the model domain. The buoyancy frequency and the theoretical solution of

¹⁴³ the first two modes of baroclinic tides are shown in the middle and right panels of Fig-

¹⁴⁴ ure 3. It can be seen that both the buoyancy frequency maximum and the first mode

¹⁴⁵ of baroclinic tide are at about 100 m depth.

¹⁴⁶ The initial ISWs fields including temperature, salinity and currents are extracted

¹⁴⁷ from the 2D simulation outputs of the ISWs in the southern Red Sea [*Guo et al.*, 2016]

¹⁴⁸ and are extrapolated into 3D fields. The location of the initial group of ISWs is indicated

¹⁴⁹ by white bold lines at the southwest corner of the domain as shown in Figure 2. A cross-

¹⁵⁰ transect (indicated by red dashed line) of the temperature field is presented in the left

¹⁵¹ panel of Figure 3, pointing to a group of well-developed ISWs with a lead wave ampli-

¹⁵² tude of more than 50 m. Five small waves follow with gradually decreasing amplitudes.

As suggested by *Vlasenko and Stashchuk* [2007], strong turbulence and mixing dur-
ing the shoaling process is expected. This motivated the use of the PP81 scheme [*Pacanowski and Philander*, 1981] to parameterize the viscosity and diffusivity,

$$\gamma = \frac{\gamma_0}{(1 + \alpha R_i)^n} + \gamma_b, \quad \kappa = \frac{\gamma}{1 + \alpha R_i} + \kappa_b, \quad (1)$$

¹⁵³ where $R_i = N^2(z)/(u_z^2 + v_z^2)$ is the Richardson number (N is the buoyancy frequency;

¹⁵⁴ u_z and v_z are the vertical shears of zonal velocity and meridional velocities, respectively).

¹⁵⁵ $\gamma_b = 10^{-5} \ m^2 s^{-1}$ and $\kappa_b = 10^{-5} \ m^2 s^{-1}$ are the background viscosity and diffusivity

¹⁵⁶ parameters, respectively. $\gamma_0 = 1.5 \times 10^{-2} \ m^2 s^{-1}, \alpha = 5$, and $n = 1$ are adjustable pa-

¹⁵⁷ rameters. The horizontal diffusivity and viscosity are set to 0.1 $m^2 s^{-1}$. This configura-

¹⁵⁸ tion provided robust simulation results in the simulation of internal solitary waves break-

¹⁵⁹ ing [*Vlasenko et al.*, 2005]. The model time-step is set to one second to satisfy the Courant-

¹⁶⁰ Friedrichs-Lewy condition. The atmospheric forcing, background currents and tidal forc-

¹⁶¹ ing are not accounted for in the simulation. The model is integrated for 28 hours and

¹⁶² its outputs are saved every 1 minute.

¹⁶³ **2.2 CMS particle tracking model**

¹⁶⁴ CMS is developed based on a stochastic, multi-scale Lagrangian framework to study

¹⁶⁵ complex larval migrations and provide probability estimates of marine population con-

¹⁶⁶ nectivity [*Paris et al.*, 2013]. Given full velocity fields, it provides a Lagrangian descrip-

¹⁶⁷ tion of oceanic phenomena (advection, dispersion, retention) and can be used in a broad

¹⁶⁸ range of applications, from the dispersion and fate of pollutants to marine spatial con-

169 servation [*Paris et al.*, 2013]. The equations based on which CMS was developed and their

170 numerical implementation are detailed in *Paris et al.* [2013], and the free open source

171 codes are available at http://code.google.com/p/connectivity-modeling-system. In this

172 study, the transport of passive particles is simulated offline with CMS based on 1-minute

173 velocity fields simulated by the MITgcm. The MITgcm-CMS system has been used to

174 study various phenomena in the Red Sea, including concentrate discharges modeling [*Zhan*

175 *et al.*, 2015], the regional-scale connectivity [*Nanninga et al.*, 2015] and basin-scale con-

176 nectivity [*Raitsos et al.*, 2017; *Wang et al.*, 2019].

177 The initial locations of particles are indicated with red dots in Figure 2, in a square

178 of 800 × 800 grids, distributed uniformly over the focus area where the ISW shoaling

179 process occurs. The distance between adjacent grid points is 450 m. Vertically, 6 lay-

180 ers at depth of 5 m, 55 m, 105 m, 155 m, 205 m, and 255 m are configured. The loca-

181 tions of these particles are saved every 1 minute.

182 Simulations at such high spatial and temporal resolution with a nonhydrostatic gen-

183 eral circulation model is computational very demanding. Using the supercomputing fa-

184 cility 'Shaheen' at KAUST, each 28-hour model simulation takes approximately 16000

185 $CPU \cdot h$, with model outputs saved every 1 minutes. Particle tracking modelling with

186 CMS is run offline based on the MITgcm outputs, with each run requiring approximately

187 3000 $CPU \cdot h$.

3 Shoaling process of ISWs

3.1 Vertical displacement of isotherms

190 The ISW shoaling process in the southern Red Sea is illustrated with the evolu-

191 tion of the displacement of the isotherm plane of 24.2 $°C$ at the depth of 90 m (Figure

192 4). The gray-scale color depicts the displacement of the isotherm plane and the white

193 color indicates the land at depth 90 m depth. Nine snapshots are presented starting at

194 T = 10.5 hours, when a group of ISWs move toward the continental slope. The first 10

195 hours are considered a spin-up period. During this process, the group of ISWs propa-

196 gates towards the slope and forms the curved-shape wave crests under dispersion and

197 side effect, as shown in Figure 4a. The curved-shape wave-crest is a common feature of

198 ISWs and has been observed by satellite images in the southern Red Sea (see Figure 1b

199 in *Guo et al.* [2016]).

–7–

The analysis of the shoaling process starts at T = 10.5 hours, when the group of ISWs exhibits complete and undisturbed wave crests. The three dashed lines indicate the vertical transects shown in Figure 5, (very similar features are observed along lines 2 and 3, and are therefore not shown), which depict the shoaling process with two convex and one concave bottom topography. One hour later, in Figure 4b, the completed curved-shape crest of the leading wave is disturbed at latitude 16.4 °N and features a remarkable horizontal anisotropy, which becomes stronger over time. The topography at the location of the disturbance suggests that the underwater seamount slows the propagation speed of the waves and leads to their refraction. In Figure 4c, at T = 12.5 hours, the leading wave starts to reach the sharp point at latitude 16.1 °N where the wave clearly steepens, with a shorten wavelength and an enlarged displacement. At T = 13.5 hours, in Figure 4d, most of the leading wave front has already encountered a convex topography and exhibits discontinuity along the wave crest. The breaking of the leading wave is observed at latitudes 16.1 °N and 16.4 °N. The wave front still propagates into the concave areas and the displacement is apparently enlarged with the along-crest energy redistribution, which is consistent with the simulation results of *Vlasenko and Stashchuk* [2007]. One hour later, the breaking of all the leading waves occur, with the following tailing waves propagating into the breaking region. An overall displacement of the isotherm plane is shown within the domain because of the wave breaking. The displacement gets stronger and occupies larger areas over time as shown in Figure 4f, g, h and i. After breaking, the wave pattern vanishes and the area is featured by an overall displacement of smaller amplitude but larger coverage. In the last panel, Figure 4i, a clear feature of wave reflection is depicted with the reflecting center point located at the concave areas, where the energy is concentrated. Some of the energy is dissipated and the rest is reflected. Meanwhile, the tail small waves are still propagating into the breaking area and follow the shoaling process.

The evolution of the horizontal velocity at 105 m depth in Figure 5 depicts similar shoaling processes. The parallel structure of velocity along the wave crest is disturbed when the wave propagates into the uneven bottom topography as shown in Figure 5, T = 11.5 h. This is followed by the appearance of complex velocity structures along various directions when the wave starts to interact with the steep slope at T = 14.5 h; the large value velocities vanish and lose their strip structures. Eventually the average velocity decreases further as the breaking process occurs in the shoaling area and some re-

flected waves starts to propagate offshore with a relatively smaller amount of energy, as shown in the last two panels of Figure 5. The two concave areas along the slope act as an amplifier to concentrate and reflect the wave energy, resulting in a group of relatively larger offshore propagating currents. The evolution of the velocity field also indicates the mechanism of the movements of particle transport, which will be discussed in Section 4.2.

3.2 Potential temperature field along wave propagation transects

Three vertical transects indicated by lines 1, 2 and 3 are plotted to depict the evolution of the temperature field during the ISW shoaling process. Twelve snapshots are shown in Figure 6. In Figure 6a, at T = 12:50, the leading ISW along line 1 propagates into the continental slope as a symmetric wave field. The trailing edge of the wave deepens over time as shown in Figure 6, at T = 13:6, 13:15 and 13:25, and some discontinuities appear at the front face of the leading wave. At T = 13:15, a bore of warm water from the surface is observed at the 100 m depth, but the generation process is absent in the previous snapshots. This indicates the occurrence of an overturning process, but the bore is formed in the nearby location across line 1 before it moves into the transect. The following snapshot in Figure 6 (T = 13:25) supports this by depicting a sharp downward intrusion of the surface water at 30 m depth. With the rear edge of the leading wave continuing to steepen at T = 13:32 and 13:39, it starts to break and form smaller waves. As revealed by the evolution of the temperature field, when the leading wave propagates into the slope, the deeper part is blocked while the shallower part continues to move forward, forming an oblique fault shape of the isotherms. This eventually evolves into a small group of water mass of a large temperature gradient at 130 m depth. One should note that the breaking process of the leading ISW is mixed with the arriving of the second ISW. As shown at T = 13:39, the front edge of the second ISW is overlapped with the post-breaking leading ISW, forming a upward polar wave structure. This second ISW follows the breaking process of the leading wave at T = 13:49, 13:59 and 14:9, until the third one reaches the slope and interacts with it. The last panel shows the temperature distribution one hour after the first three ISWs break and disintegrate into a group of smaller waves. The following waves keep propagating into the breaking area and absorb the energy left by the leading waves after their breaking. This results in larger displacement of isotherms and creates intensified overturning and breaking.

Combining the waves breaking process with the parameters of the leading wave slope Sw of about 0.07 and the topography slope S of about 0.01, the shoaling process is found to follow a mild breaking process. In this process, the slow steepening of the rear face of the wave occurs following the slow change of the water depth, but remains insufficient to form a collapsing. Instead, a positive tail forms behind and locally moves the interface upward, causing the transformation of wave polarity as it moves onshore. With the step-like structure followed, the group of waves eventually evolve into smaller bores and dissipate. During this process, the boundary layer separation and overturning also occur over shorter time scales. All of these processes are well reproduced in our simulation results.

Comparing the transects along the three lines, no clear difference other than an observed time-lag during the ISWs breaking process, indicating that the along wave-crest redistribution of wave energy due to the 3D variation of bottom topography does not result in a significant change of the wave breaking type. Thus, the evolution of transects line 2 and line 3 is not presented here. *Guo et al.* [2016] investigated and described the 2D ISW shoaling process in the southern Red Sea. This study improved on the 2D experiment of *Guo et al.* [2016] by removing the background barotropic tidal velocities to examine the shoaling process. The 2D study presents a similar evolution process, despite the limitations of a 2D setup and the presence of background barotropic tides (in *Guo et al.* [2016]), particularly in term of the mild breaking process without significant overturning of stratification, as well as the reflected low-amplitude wave after shoaling. The 2D simulations do not however well reproduce the onshore propagating small group of waves in details, showing instead a relatively more complex mixing process and more energy reflected and resulting in recognisable waves propagating offshore, which is possibly due to the alongshore energy redistribution in the present 3D setting.

3.3 Evolution of wave energy

The wave energy, E, is the sum of the kinetic energy (KE) $\int_V 1/2\rho(u^2+v^2+w^2)dV$ and the potential energy (PE) $\int_V \rho gz dV$, which can also be divided into the background potential energy (BPE) $g\int_V \rho z_\star dV$ and available potential energy (APE) $g\int_V \rho(z-z_\star)dV$, where $z_\star$ gives the vertical position in the reference state of the fluid parcel [*Winters et al.*, 1995]. Since the BPE does not depend on the parameters of the incoming wave and describes only the potential energy due to background stratification, and thus cannot con-

vert into kinetic energy and ultimately into heat [*Vlasenko and Stashchuk*, 2007; *Lamb*, 2007, 2008], here we consider the total wave energy E as the sum of KE and APE.

The energy is calculated based on the area integral with the initial time at 10.5 hours, corresponding to the first snapshot shown in Figure 4. Their dependence on time during the ISW shoaling process is presented in Figure 7, with red curve indicating the APE, blue curve indicating the KE, and black dash curve showing the total wave energy. Consistently, as a mild breaking process, the 'fission' process preserves about 65% of its total energy during the overall shoaling process, as some of the large amplitude ISWs are converted into smaller waves and do not dissipate eventually during the process. The KE and APE contribute evenly to the dissipation and loss of the total wave energy, about 16% from KE and 19% from APE. However, the KE presents a sharp loss of energy at the beginning of the breaking process before it levels off, while the APE shows a mild and fixed gradient rate of loss of energy throughout the process. This is also consistent with the mild breaking process, as at the beginning when the first ISW meets the slope and gets blocked, the large velocities dissipate rapidly, while the following smaller waves with a relatively weak velocities do not significantly contribute to this process. The loss of potential energy occurs at a mild constant rate because the alternation of stratification is present during the whole process.

4 Particle transport tracking results

4.1 General characteristics

Based on the outputs of the MITgcm, particles transport experiments are conducted during the ISW shoaling process in the southern Red Sea using CMS. As described in Subsection 2.2, the particles are released at six different depths of 5 m, 55 m, 105 m, 155 m, 205 m and 255 m. The analysis first focuses on the particles transport at the different layers.

Eight snapshots of the locations of the particles released at 5 m depth are presented in Figure 8a, overlayed with the bottom topography indicated with gray-scale color-bar and the depth of particles indicated with jet color-bar. The first snapshot is plotted at T = 12 h, before the propagation of the leading wave into the shoal (see in Figure 4b and c). A clear feature is depicted showing the particles modulated into a few strips by the ISWs. This is due to the internal wave-induced convergence and divergence move-

–11–

ments of water in the surface, which makes it detectable from satellite images [*Alpers*, 1985]. Two hours later, at T = 14 h, the breaking of the leading wave occurs, causing a complex upward and downward transports of particles, as indicated by mixed red and blue color dots. At T = 16 h, 18 h and 20 h, as the following waves continue arriving the slope and break, the mixing processes keep intensifying the transport. Strips of impacted particles are presented on the shallow shelf from T = 18 h and 20 h, and these particles gradually settle as shown at T = 22 h and 24 h. A gap strip with less particles along the shelf break presents. The gap becomes larger over time, and only a small number of particles stay in the initial layer at 5 m depth. The average vertical transported depth of these particles released at the surface is about 5-10 m. Another noticeable feature is the reflected solitary wave with a more curvy crest and smaller amplitude, as indicated by the stripe of particles at T = 20 h, 22 h and 24 h.

Figure 9 presents the transport of particles initiated at 55 m depth. Compared to Figure 8, the wave-shape strips of particles concentration is more obvious and the vertical movement is stronger, as the displacements of isotherm are larger at this depth as compared to the surface. However, the strips gradually disappear after the waves pass through. At time T = 18 h, the strip-shape can be hardly recognized. Consistently, the vertical movement of the 55 m particles at the breaking area is much stronger than that of the 5 m particles. These particles are transported downward and can reach depths deeper than 100 m, while the particles moving upward can reach 10 m and above. One noticeable difference with the particles released at 5m is the no apparent 'gap' present compared to that in Figure 8. Instead, a concentration of particles is observed where most of them are transported upward to the surface and downward to the bottom, while moving horizontally along the wave-crest.

The particles released at 105 m follows a similar process to that of the particles released at 55 m, except for less particles along the shelf break after the breaking process at T = 24 h and 26 h. This is partly due to the nature of the CMS model which assigns a NAN value to the particles shading at the land points. The movements of the particles released at 155 m (not shown) resemble those of the particles released at 105 m. At T = 26 h, most of the particles settle near the depth of 155 m other than the particles within the breaking area.

–12–

The particles initiated at deeper layers present similar movements, as shown in Figure 11 for 205 m particles (similar at 255 m,not shown). A noticeable difference is the particles from deep layers being more affected by the bottom topography as indicated by the final settled pattern of these particles.

4.2 Along propagation transects

More results can be inferred from the trajectories of the particles movements along the propagation transects, as seen in Figure 12 showing the particles' horizontal movements and in Figure 13 showing the particles vertical movements at six different layers, respectively. The color here indicates the time in hours during the shoaling process. In Figure 12, the movements of the particles from the surface (5 m) and mid depth (55 m and 105 m) exhibits more horizontal movements compared to the particles released at the bottom layer depths (155 m, 105 m and 155 m). The figure shows clear firstly an onshore movements to the northeast while an offshore movement after 14h for the upper layer particles. The pattern is consistent while the amplitude of the particles movement is decreased with depth. This feature can be interpreted from the evolution of the horizontal velocity field shown in Figure 5. When the large velocities vanish at the shoaling area, some of the energy is reflected and propagates offshore at a relatively smaller speed, as seen in the last panel in Figure 5.

A vertical view of particles movements along the transect at different layers is presented in Figure 13. Similar to the above vertical distribution analysis, a stronger vertical transport is observed near the wave breaking point (near 41.7 ° E) with a large number of particles dragged down and a small part up due to the strong mixing processes, as seen in the panel from particles released at 5 m. A noticeable shore-ward movement is also observed for these downward transported particles after the breaking process. Particles released at 55 m show stronger vertical movements, with the maximum vertical transport distance of about 30 m. For 105 m particles, the vertical transport distance is even larger (about 40 m), however, with a small portion of particles propagating upward. Particles released at the lower layers exhibits similar movements to the mid-depth layers particles, with a vertical transport distance within 20 m both upward and 30 m downward. The particles initiated at 255 m follow different movement pattern during the late period (T = 14-20 h), indicating that the reflected waves are more affected by the bottom topography, which is consistent with the Figure 11. Vertical oscillations occasionally oc-

–13–

³⁹¹ cur for all-layer particles, with amplitude gradually decreasing with time, as indicated

³⁹² by the blue-yellow-red trajectories.

³⁹³   *Arthur and Fringer* [2016] investigated the particles transported onshore and off-

³⁹⁴ shore by the breaking of internal waves, revealing in particular that the particles are con-

³⁹⁵ centrated along the pcynocline as they propagate offshore together with the relaxed up-

³⁹⁶ slope surge. This resembles the Intermediate Nepheloid Layer (INL) [*McPhee-Shaw et al.*,

³⁹⁷ 2004; *McPhee-Shaw*, 2006]. However, in this study, the INL is not apparent even though

³⁹⁸ the offshore transport of particles is observed at the mid-depth and bottom. This could

³⁹⁹ partly be due to the non-continuous vertical setup of particles, and because of the rel-

⁴⁰⁰ atively coarse vertical resolution of our model configuration.

4.3 Vertical distribution

⁴⁰²   The vertical distribution of particles is also analyzed statistically over time. In Fig-

⁴⁰³ ure 14, the left panels display the vertical distribution of the particles initiated at dif-

⁴⁰⁴ ferent layers. The associated histograms at the last snapshot T = 27.5 hours are shown

⁴⁰⁵ accordingly in the right six panels. Figure 15 depicts the same distribution but with the

⁴⁰⁶ particles released only within the breaking area (calculation based on the white rectan-

⁴⁰⁷ gular in Figure 2). The frequency (portion) of particles in each plot is provided in the

⁴⁰⁸ corresponding captions. Figure 14 shows that most of the particles initiated at 5 m depth

⁴⁰⁹ remain at the surface, and reach a maximum depth of 40 m. The histogram of the last

⁴¹⁰ snapshot suggests that after the breaking process, most of the particles released at 5 m

⁴¹¹ are distributed at 0-5 m (42 %) and 5-10 m (56 %), while a very small portion of them

⁴¹² reaching 20-40 m depths. The particles released at 55 m show more vertical movements

⁴¹³ than those released at the surface. They reach a maximum depth of about 100 m. Even

⁴¹⁴ though a maximum portion of particles ($\sim$ 90 %) stay within 40-60 m depth, a small por-

⁴¹⁵ tion is settled in the upper layer (10-30 m), and so as the lower layer (70-80 m). The par-

⁴¹⁶ ticles initiated at 105 m show similar features to those released at 55 m. Most of the par-

⁴¹⁷ ticles are settled within 10 m both upward and downward away from the initiated depth,

⁴¹⁸ after that they all experience an oscillation with maximum depth of about 30 m. An-

⁴¹⁹ other feature that can be observed in the left panels suggests a clear downward move-

⁴²⁰ ments occurring for all layer particles as around T = 9 h, as they are affected by the waves.

⁴²¹ Both upward and downward transports are then found at around T = 14 h, when the

⁴²² leading waves start to break and cause vertical mixing.

–14–

The vertical distribution of particles in the breaking area resembles that of the overall particles, with more prominent maximum values, especially for the particles initiated at 55 m and 105 m. More particles are settled more than 10 m vertically away from their release depth. It should be noted that the breaking area defined here is the white rectangular shown in Figure 2, which includes some of the shelf area and some with deeper depths, instead of following the curve of shelf break. This could explain, to some extent, the similar pattern of the particles in the overall area and breaking area.

4.4 Transport distance

Two types of transport distance are also calculated with T_s referring to the distance between the location of the last snapshot at T = 27.5 hours and the initial location, and T_i referring to the temporally integrated distance over the whole process. The histograms of the corresponding horizontal and vertical distributions are shown in Figures 16 and 17, respectively.

For the overall particles, the horizontal T_s exhibits a slightly skewing Gaussian distribution with the main peak near 800 m, a maximum frequency of 0.11, and secondary peak near 2000 m, a frequency of 0.04. The maximum distance reaches up to 4000 m. The horizontal T_s of the particles in the breaking area shows a maximum value of near 0.09 at 300 m while exhibits a more evenly-distribution for the distances between 1000 m and 5000 m, with a maximum value at about 2000 m with a frequency of 0.025. The percentage of particles from the breaking area travelling between 3000 m to 4000 m is apparently larger than that of the overall particles. Vertically, the overall particles and those in the breaking area exhibit very similar distributions, with 0 to 10 m taking the maximum values and a sharp decreasing towards the maximum transport distance of about 40 m. Slightly more particles in the breaking area are transported at distance of 10-30 m compared to the overall particles, consistent with the more complex breaking and mixing process occurring in this area.

The T_i presents quite different features than those of T_s, as shown in Figure 17. The horizontal distribution of T_i for the overall particles shows one dominant peak at distance around 2000, with maximum value of 0.105, and relatively even-distributed for the distance from 5000 to 10000 m. For the particles inside the breaking area, the peak remains at 1000 m, while it shows another peak at around 5800 m. Vertically, the over-

all particles exhibit an extreme value at around 40 m and then a mild Gaussian's distribution with peak at around 500 m. For the particles inside the breaking area, it shows a similar peak at around 300 m, while a small but not neglectable portion of particles travel a distance between 2000 m and 6000 m. One noticeable point is the horizontal T_i being almost double of the T_s, while this reaches more than 20 times in the vertical. This indicates that the particles experience intensified vertical movements, especially for the particles inside the breaking area.

5 Summary

Satellite images revealed the southern Red Sea as a new hot spot for ISWs. The shoaling process of these waves has a significant influence on the particle transport, such as nutrients, sediments and larvae, which are important for the regional marine ecosystem. A 3D, non-hydrostatic, high-resolution MITgcm configured with a realistic topography and ocean conditions has been used to simulate the shoaling process of a group of ISWs in this region. The breaking and dissipation processes are well simulated. Combining the wave breaking process with the parameters of the leading wave slope Sw of about 0.07 and the topography slope S of about 0.01, the shoaling mechanism is suggested to follow a mild breaking process. In this process, the slow steepening of the rear face of the wave occurs following the slow change of the water depth, but still insufficient to form a collapsing. Instead, a positive tail forms behind and locally moves the interface upward, causing the transformation of wave polarity as it moves onshore. With the step-like structure followed, the group of waves eventually evolve into smaller water bores and dissipate. During this process, the boundary layer separation and overturning also occur over shorter time scales. All of these processes are well reproduced in our simulation results.

Based on the MITgcm outputs, the particles transport during the shoaling process is examined using CMS. 38400 particles were released on six different layers in the main shoaling domain. Snapshots of particles locations show that, in the domain outside the breaking area, most of the particles are transported up-and-down following the wave oscillation process then settle within 10-20 m around the original released depth. For the particles inside the breaking area, the oscillation process becomes more complex and intensified, and eventually a great portion of these particles settle far away from their released locations. The redistribution process also varies with depth. Particles at mid-layer

–16–

depth are more likely influenced by the waves than the particles from the surface and the bottom. The settlements of particles from the low-layers are more affected by the bottom topography.

Histogram of travel distance T_s for the overall particles and within the breaking area show similar distribution patterns, while the particles within the breaking area exhibit a slightly larger portion at longer distances both horizontally and vertically. The time-integrated travel distance T_i revealed similar results, which is consistent with the complex and intensified processes within the breaking area. For the particles inside the breaking area, T_i is 20 times larger than T_s in the vertical and more than 2 times in the horizontal, indicating that these particles experience a continuous vertical transport.

References

Aghsaee, P., L. Boegman, and K. G. Lamb (2010), Breaking of shoaling internal solitary waves, *J. Fluid Mech.*, *659*, 289–317, doi:10.1017/S002211201000248X.

Alford, M. H., T. Peacock, J. A. MacKinnon, J. D. Nash, M. C. Buijsman, L. R. Centurioni, S.-Y. Chao, M.-H. Chang, D. M. Farmer, O. B. Fringer, et al. (2015), The formation and fate of internal waves in the south china sea, *Nature*, *521*(7550), 65.

Alpers, W. (1985), Theory of radar imaging of internal waves, *Nature*, *314*(6008), 245.

Arthur, R. S., and O. B. Fringer (2014), The dynamics of breaking internal solitary waves on slopes, *J. Fluid Mech.*, *761*(2), 360–398, doi:10.1017/jfm.2014.641.

Arthur, R. S., and O. B. Fringer (2016), Transport by breaking internal gravity waves on slopes, *J. Fluid Mech.*, *789*, 93–126, doi:10.1017/jfm.2015.723.

Berumen, M. L., A. Hoey, W. H. Bass, J. Bouwmeester, D. Catania, J. E. Cochran, M. T. Khalil, S. Miyake, M. Mughal, J. L. Spät, et al. (2013), The status of coral reef ecology research in the red sea, *Coral Reefs*, *32*(3), 737–748.

Boegman, L., G. N. Ivey, and J. Imberger (2005), The degeneration of internal waves in lakes with sloping topography, *Limnol. Oceanogr.*, *50*(5), 1620–1637, doi:10.4319/lo.2005.50.5.1620.

Bogucki, D., T. Dickey, and L. G. Redekopp (1997), Sediment Resuspension and Mixing by Resonantly Generated Internal Solitary Waves, *J. Phys. Oceanogr.*, *27*(7), 1181–1196, doi:10.1175/1520-0485(1997)027¡1181:SRAMBR¿2.0.CO;2.

Bourgault, D., and D. E. Kelley (2007), On the Reflectance of Uniform Slopes for Normally Incident Interfacial Solitary Waves, *J. Phys. Oceanogr.*, *37*(5), 1156–1162, doi:10.1175/JPO3059.1.

Carter, G. S., M. C. Gregg, and R. C. Lien (2005), Internal waves, solitary-like waves, and mixing on the Monterey Bay shelf, *Cont. Shelf Res.*, *25*(12-13), 1499–1520, doi:10.1016/j.csr.2005.04.011.

Da Silva, J., J. Magalhaes, T. Gerkema, and L. Maas (2012), Internal Solitary Waves in the Red Sea: An Unfolding Mystery, *Oceanography*, *25*(2), 96–107, doi:10.5670/oceanog.2012.45.

Davis, K. A., and S. G. Monismith (2011), The Modification of Bottom Boundary Layer Turbulence and Mixing by Internal Waves Shoaling on a Barrier Reef, *J. Phys. Oceanogr.*, *41*(11), 2223–2241, doi:10.1175/2011JPO4344.1.

Droghei, R., F. Falcini, D. Casalbore, E. Martorelli, R. Mosetti, G. Sannino, R. Santoleri, and F. Chiocci (2016), The role of internal solitary waves on deep-water sedimentary processes: the case of up-slope migrating sediment waves off the messina strait, *Scientific reports*, *6*, 36,376.

Garrett, C., and E. Kunze (2007), Internal Tide Generation in the Deep Ocean, *Annu. Rev. Fluid Mech.*, *39*(1), 57–87, doi: 10.1146/annurev.fluid.39.050905.110227.

Gladstone, W. (1996), Unique annual aggregation of longnose parrotfish (hipposcarus harid) at farasan island (saudi arabia, red sea), *Copeia*, *1996*(2), 483–485.

Guo, C. (2013), Investigation of baroclinic tides in the northern south china sea (doctoral dissertation, university of plymouth).

Guo, D., T. R. Akylas, P. Zhan, A. Kartadikaria, and I. Hoteit (2016), On the generation and evolution of internal solitary waves in the southern Red Sea, *J. Geophys. Res. Ocean.*, *121*(12), 8566–8584, doi:10.1002/2016JC012221.

Helfrich, K. R., and J. Pineda (2003), Accumulation of particles in propagating fronts, *Limnol. Oceanogr.*, *48*(4), 1509–1520, doi:10.4319/lo.2003.48.4.1509.

Hosegood, P., J. Bonnin, and H. van Haren (2004), Solibore-induced sediment resuspension in the Faeroe-Shetland channel, *Geophys. Res. Lett.*, *31*(9), doi: 10.1029/2004GL019544.

Klymak, J. M., and J. N. Moum (2003), Internal solitary waves of elevation advancing on a shoaling shelf, *Geophys. Res. Lett.*, *30*(20), n/a–n/a, doi: 10.1029/2003GL017706.

La Forgia, G., C. Adduce, and F. Falcini (2018a), Laboratory investigation on internal solitary waves interacting with a uniform slope, *Advances in Water Resources*, *120*, 4–18.

La Forgia, G., T. Tokyay, C. Adduce, and G. Constantinescu (2018b), Numerical investigation of breaking internal solitary waves, *Physical Review Fluids*, *3*(10), 104,801.

La Forgia, G., T. Tokyay, C. Adduce, and G. Constantinescu (2020), Bed shear stress and sediment entrainment potential for breaking of internal solitary waves, *Advances in Water Resources*, *135*, 103,475.

Lamb, K. G. (2007), Energy and pseudoenergy flux in the internal wave field generated by tidal flow over topography, *Continental shelf research*, *27*(9), 1208–1232.

Lamb, K. G. (2008), On the calculation of the available potential energy of an isolated perturbation in a density-stratified fluid, *Journal of Fluid Mechanics*, *597*, 415.

Leichter, J. J., S. R. Wing, S. L. Miller, and M. W. Denny (1996), Pulsed delivery of subthermocline water to Conch Reef (Florida Keys) by internal tidal bores, *Limnol. Oceanogr.*, *41*(7), 1490–1501, doi:10.4319/lo.1996.41.7.1490.

Leichter, J. J., H. L. Stewart, and S. L. Miller (2003), Episodic nutrient transport to Florida coral reefs, *Limnol. Oceanogr.*, *48*(4), 1394–1407, doi: 10.4319/lo.2003.48.4.1394.

Marshall, J., A. Adcroft, C. Hill, L. Perelman, and C. Heisey (1997), A finite-volume, incompressible navier stokes model for studies of the ocean on parallel

583   computers, *Journal of Geophysical Research: Oceans*, *102*(C3), 5753–5766.

584   McPhee-Shaw, E. (2006), Boundary–interior exchange: reviewing the idea that

585   internal-wave mixing enhances lateral dispersal near continental margins, *Deep*

586   *Sea Research Part II: Topical Studies in Oceanography*, *53*(1-2), 42–59.

587   McPhee-Shaw, E., R. Sternberg, B. Mullenbach, and A. Ogston (2004), Observations

588   of intermediate nepheloid layers on the northern california continental margin,

589   *Continental Shelf Research*, *24*(6), 693–720.

590   Michallet, H., and G. N. Ivey (1999), Experiments on mixing due to internal soli-

591   tary waves breaking on uniform slopes, *J. Geophys. Res.*, *104*(C6), 13,467–13,477,

592   doi:10.1029/1999JC900037.

593   Nanninga, G. B., P. Saenz-Agudelo, P. Zhan, I. Hoteit, and M. L. Berumen (2015),

594   Not finding nemo: limited reef-scale retention in a coral reef fish, *Coral Reefs*,

595   *34*(2), 383–392.

596   Omand, M. M., J. J. Leichter, P. J. Franks, R. T. Guza, A. J. Lucas, and F. Fed-

597   dersen (2011), Physical and biological processes underlying the sudden surface

598   appearance of a red tide in the nearshore, *Limnol. Oceanogr.*, *56*(3), 787–801,

599   doi:10.4319/lo.2011.56.3.0787.

600   Pacanowski, R., and S. Philander (1981), Parameterization of vertical mixing in

601   numerical models of tropical oceans, *Journal of Physical Oceanography*, *11*(11),

602   1443–1451.

603   Paris, C. B., J. Helgers, E. Van Sebille, and A. Srinivasan (2013), Connectivity mod-

604   eling system: A probabilistic modeling tool for the multi-scale tracking of biotic

605   and abiotic variability in the ocean, *Environmental Modelling & Software*, *42*,

606   47–54.

607   Pineda, J. (1994), Internal tidal bores in the nearshore: Warm-water fronts, sea-

608   ward gravity currents and the onshore transport of neustonic larvae, *J. Mar. Res.*,

609   *52*(3), 427–458, doi:10.1357/0022240943077046.

610   Pineda, J. (1995), An internal tidal bore regime at nearshore stations along west-

611   ern U.S.A.: Predictable upwelling within the lunar cycle, *Cont. Shelf Res.*, *15*(8),

612   1023–1041, doi:10.1016/0278-4343(95)80007-Z.

613   Pineda, J. (1999), Circulation and larval distribution in internal tidal bore warm

614   fronts, *Limnol. Oceanogr.*, *44*(6), 1400–1414, doi:10.4319/lo.1999.44.6.1400.

Quaresma, L. S., J. Vitorino, A. Oliveira, and J. da Silva (2007), Evidence of sediment resuspension by nonlinear internal waves on the western Portuguese mid-shelf, *Mar. Geol.*, *246*(2-4), 123–143, doi:10.1016/j.margeo.2007.04.019.

Raitsos, D. E., R. J. Brewin, P. Zhan, D. Dreano, Y. Pradhan, G. B. Nanninga, and I. Hoteit (2017), Sensing coral reef connectivity pathways from space, *Scientific Reports*, *7*(1), 9338.

Riegl, B. M., A. W. Bruckner, G. P. Rowlands, S. J. Purkis, and P. Renaud (2012), Red sea coral reef trajectories over 2 decades suggest increasing community homogenization and decline in coral size, *PLoS One*, *7*(5), e38,396.

Scotti, A., R. C. Beardsley, B. Butman, and J. Pineda (2008), Shoaling of nonlinear internal waves in massachusetts bay, *Journal of Geophysical Research: Oceans*, *113*(C8).

Simmons, H. L., S. R. Jayne, L. C. St. Laurent, and A. J. Weaver (2004), Tidally driven mixing in a numerical model of the ocean general circulation, *Ocean Model.*, *6*(3-4), 245–263, doi:10.1016/S1463-5003(03)00011-8.

Sutherland, B., K. Barrett, and G. Ivey (2013), Shoaling internal solitary waves, *Journal of Geophysical Research: Oceans*, *118*(9), 4111–4124.

Venayagamoorthy, S., and O. Fringer (2006), Numerical simulations of the interaction of internal waves with a shelf break, *Physics of Fluids*, *18*(7), 076,603.

Venayagamoorthy, S. K., and O. B. Fringer (2007), On the formation and propagation of nonlinear internal boluses across a shelf break, *J. Fluid Mech.*, *577*, 137–159, doi:10.1017/S0022112007004624.

Vlasenko, V., and K. Hutter (2002), Numerical Experiments on the Breaking of Solitary Internal Wavesover a SlopeShelf Topography, *J. Phys. Oceanogr.*, *32*(6), 1779–1793, doi:10.1175/1520-0485(2002)032¡1779:NEOTBO¿2.0.CO;2.

Vlasenko, V., and N. Stashchuk (2007), Three-dimensional shoaling of large-amplitude internal waves, *Journal of Geophysical Research: Oceans*, *112*(C11).

Vlasenko, V., N. Stashchuk, and K. Hutter (2005), *Baroclinic tides: theoretical modeling and observational evidence*, Cambridge University Press.

Wallace, B. C., and D. L. Wilkinson (1988), Run-up of internal waves on a gentle slope in a two-layered system, *J. Fluid Mech.*, *191*, 419–442, doi: 10.1017/S0022112088001636.

Walter, R. K., C. Brock Woodson, R. S. Arthur, O. B. Fringer, and S. G. Monismith (2012), Nearshore internal bores and turbulent mixing in southern Monterey Bay, *J. Geophys. Res. Ocean.*, *117*(7), doi:10.1029/2012JC008115.

Walter, R. K., C. B. Woodson, P. R. Leary, and S. G. Monismith (2014), Connecting wind-driven upwelling and offshore stratification to nearshore internal bores and oxygen variability, *J. Geophys. Res. Ocean.*, *119*(6), 3517–3534, doi: 10.1002/2014JC009998.

Wang, Y., D. E. Raitsos, G. Krokos, J. A. Gittings, P. Zhan, and I. Hoteit (2019), Physical connectivity simulations reveal dynamic linkages between coral reefs in the southern red sea and the indian ocean, *Scientific reports*, *9*(1), 1–11.

Winters, K. B., P. N. Lombard, J. J. Riley, and E. A. D'Asaro (1995), Available potential energy and mixing in density-stratified fluids, *Journal of Fluid Mechanics*, *289*, 115–128.

Zhan, P., F. Yao, A. R. Kartadikaria, Y. Viswanadhapalli, G. Gopalakrishnan, and I. Hoteit (2015), Far-field ocean conditions and concentrate discharges modeling along the saudi coast of the red sea, in *Intakes and Outfalls for Seawater Reverse-Osmosis Desalination Facilities*, pp. 501–520, Springer.

664 **Figures**
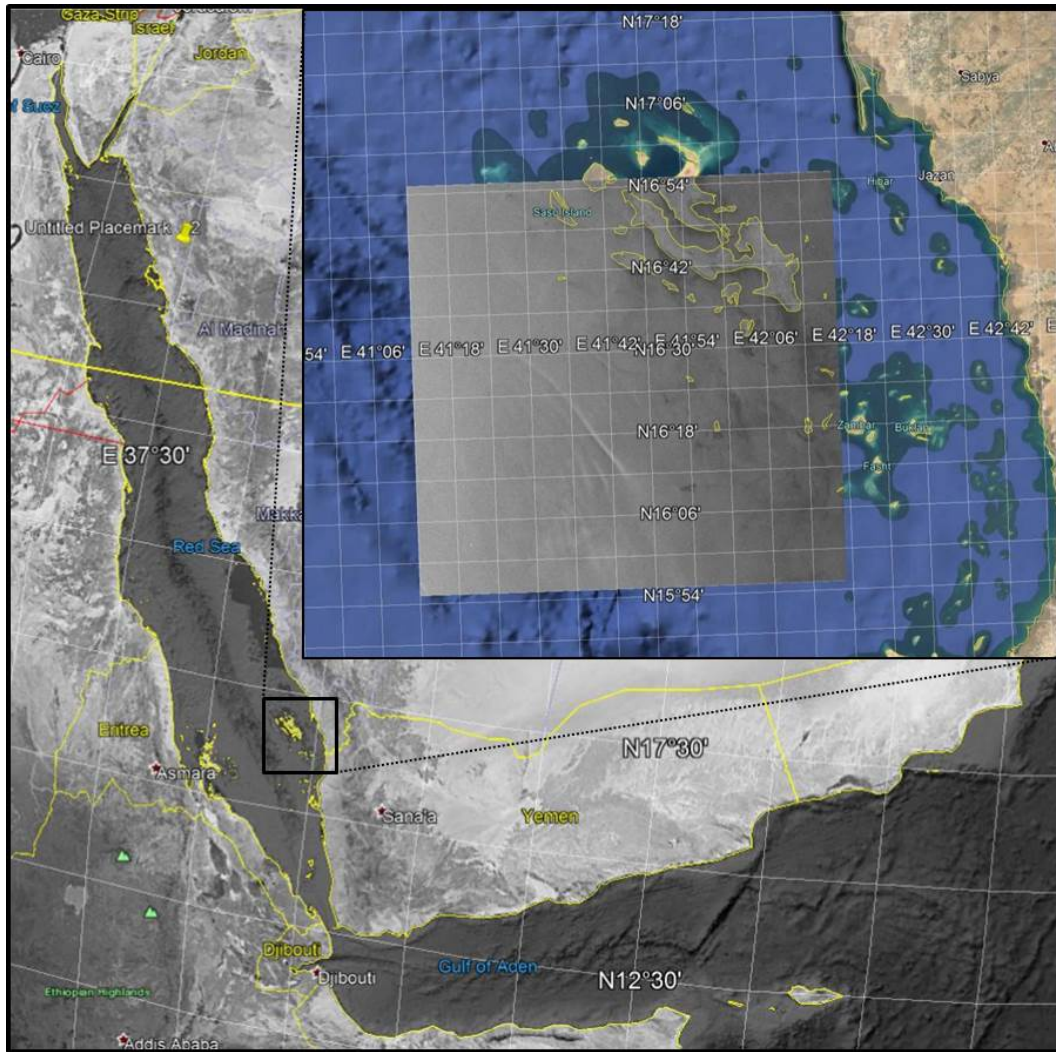
665 **Figure 1.** Satellite images observing ISWs in the southern Red Sea, overlapped with the
666 bottom topography.

Figure 2. Bottom topography of the model domain. Curved lines with labels indicate the iso-baths. Five white thick lines indicate the initialized group of ISWs and the red dashed line show the ISWs propagation axis. The square of red dots show the locations of the particles released and the white rectangular indicates the area ISWs breaks.
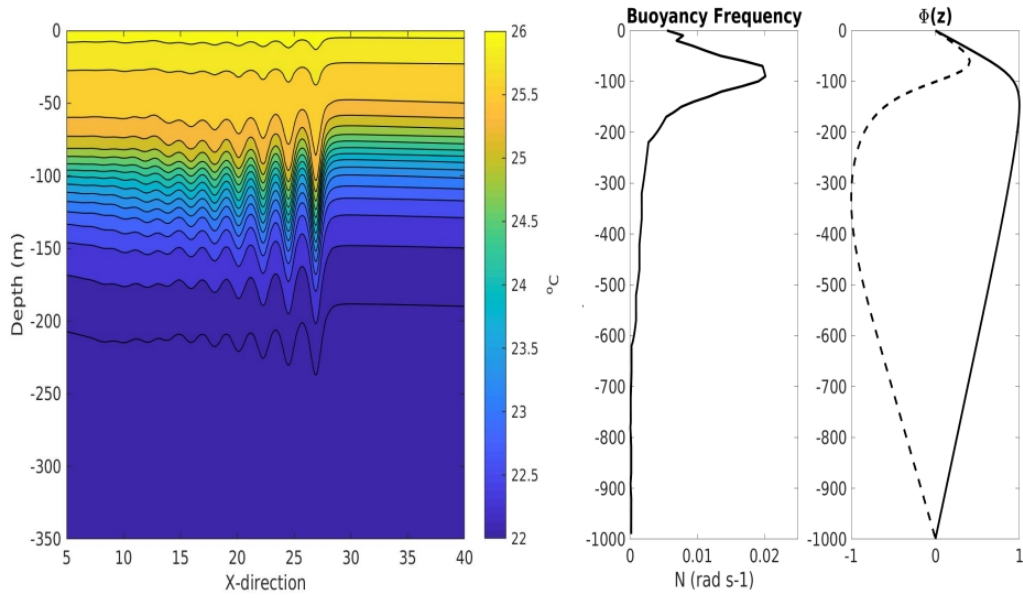
671 **Figure 3.** Initial ISWs fields. Left panel shows the initial temperature field of the cross-

672 section indicated by red dashed line in Figure 2. The model configured buoyancy frequency and

673 the theoretical solution of the first-two baroclinic tides are shown in the middle and right panel,

674 respectively.
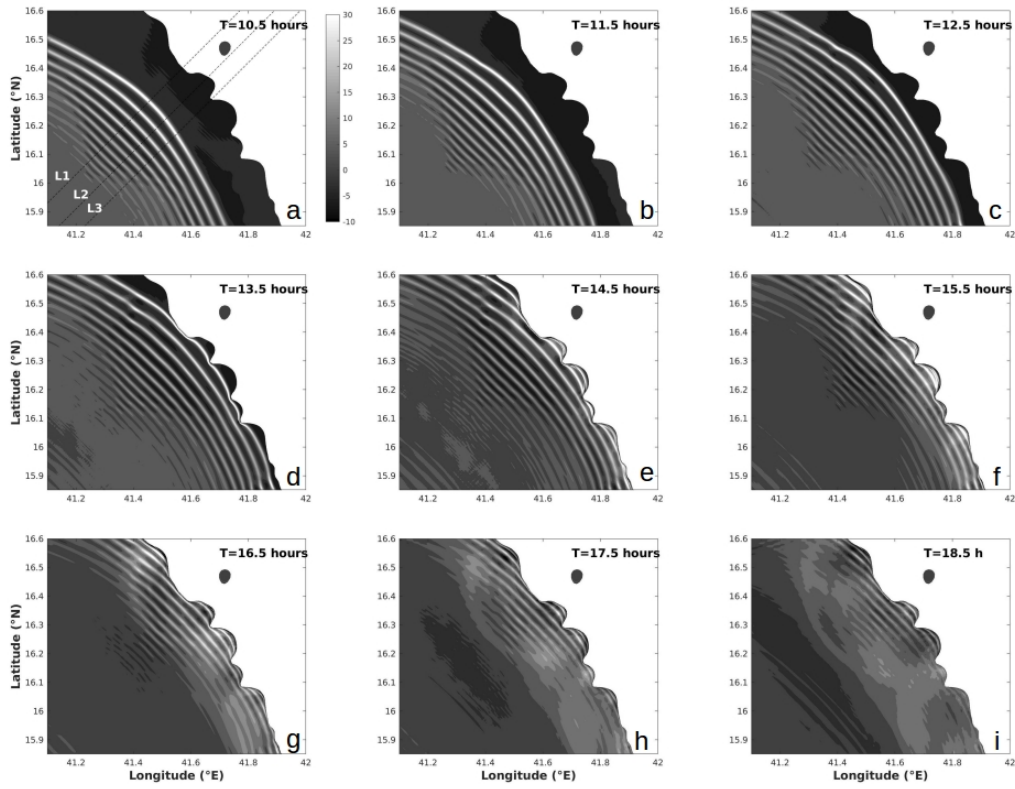
Figure 4. Nine snapshots of $24.2°C$ isotherm displacement during the ISW shoaling process, at the depth of 90 m. In the first plot, three dashed lines L1, L2 and L3 indicate the transects along the wave propagation directions.
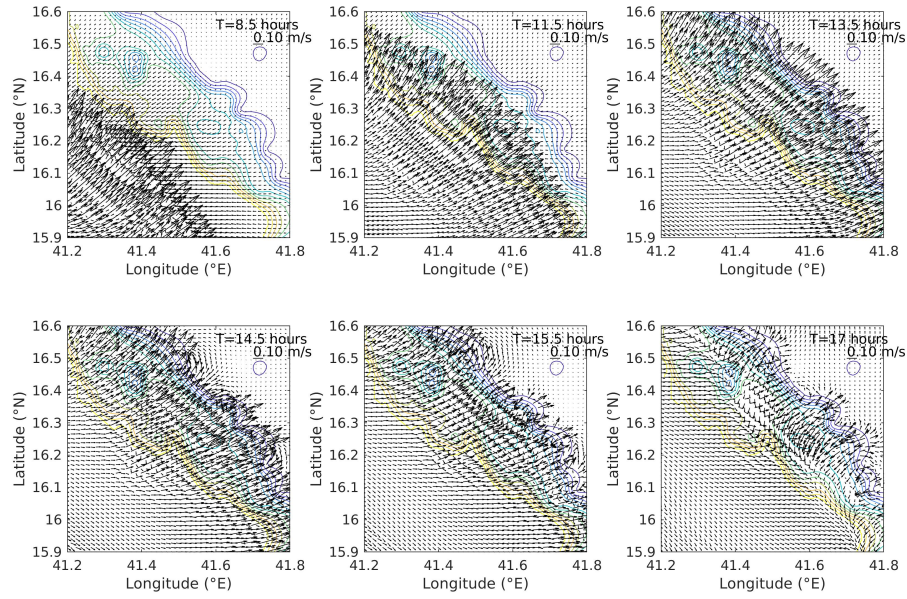
Figure 5. Six snapshots of horizontal velocity field at the depth of 105 m, overlapped with the bottom topography.
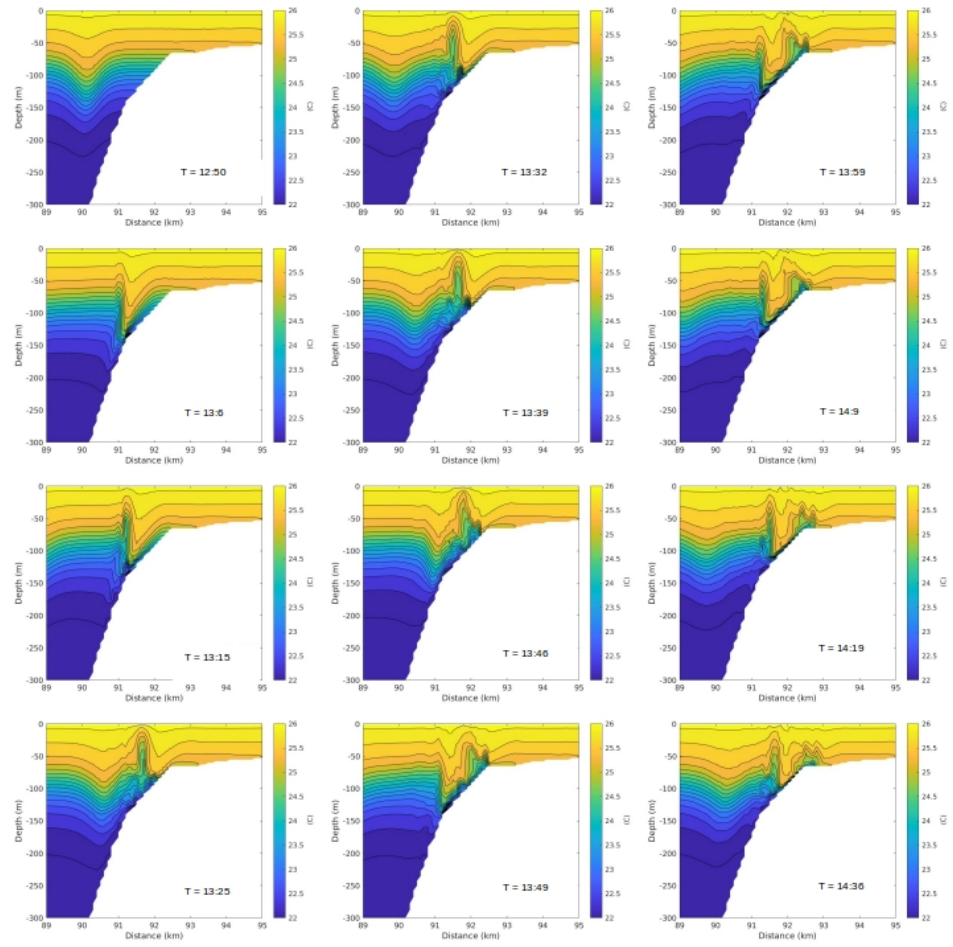
Figure 6. Twelve snapshots of potential temperature field along the transect L1 during the

ISW shoaling process. Location of line 1 is indicated in Figure 4a.

–28–

682 **Figure 7.** Dependence of the kinetic energy (blue curve), potential energy (red curve), and

683 their integration (black dash curve) over time during the shoaling process of ISWs, normalized by

684 the initial value of total energy at 10.5 hours.

685 **Figure 8.** Eight snapshots of the locations of particles initiated at 5 m depth, overlapped with

686 bottom topography. The bottom topography is indicated with gray-scale color and the depth of

687 particles is shown with jet color-bar.

688 **Figure 9.** Same with Figure 8 but with particle initial depth at 55 m.

689 **Figure 10.** Same with Figure 8 but with particle initial depth at 105 m.

690 **Figure 11.** Same with Figure 8 but with particle initial depth at 205 m.

691 **Figure 12.** Horizontal trajectories of particles along the transect L2, at six vertical layers

692 during the ISW shoaling process, overlapped with bottom topography. Jet color-bar indicates the

693 time in hours.

Figure 13. Vertical trajectories of particles along the transect L2, at six vertical layers during the ISW shoaling process, with black bold curve indicating the bottom topography. Jet color-bar indicates the time in hours.

–35–
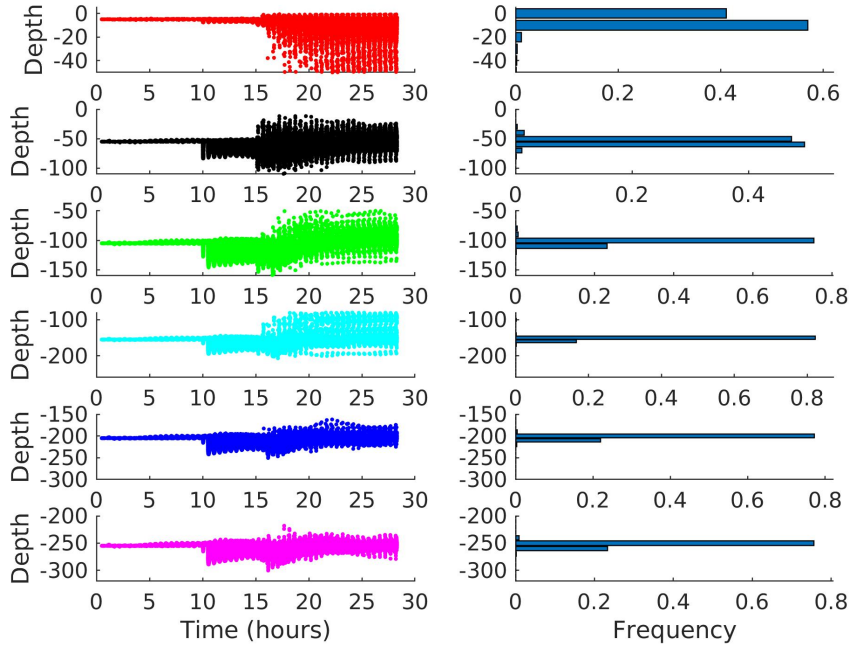
Figure 14. Left six panels: vertical distribution of particles over time, for initial depth of 5 m, 55 m, 105 m, 155 m, 205 m and 255 m, respectively. Right six panels: histogram of vertical distribution of particles at time T = 27.5 hours. All the particles within the red square (see in Figure 2) are used. The numbers of particles initiated at different layers are 6364, 4641, 3611, 3480, 3252 and 2919, respectively.
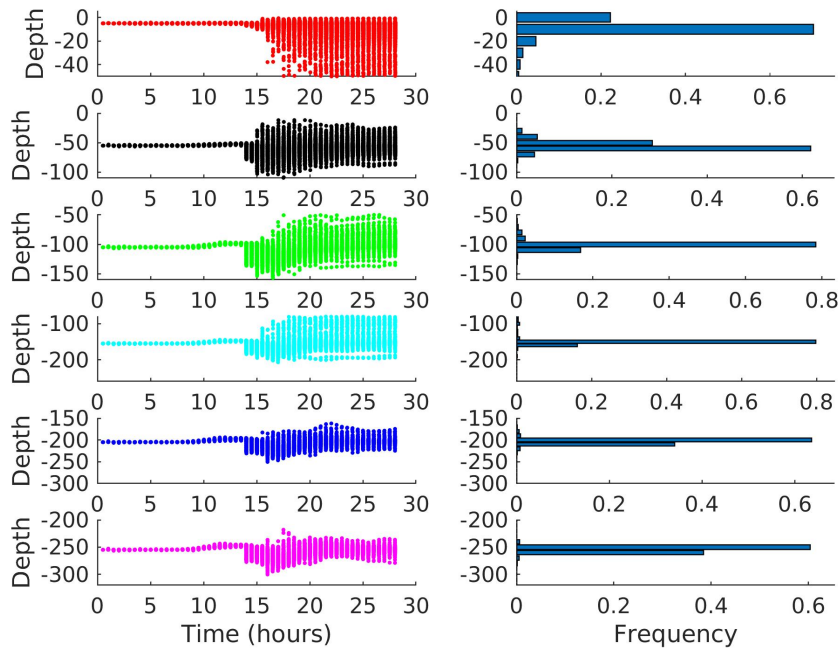
Figure 15. Same with Figure 14 but using particles only within the white rectangular in Figure 2. The numbers of particles initiated at different layers are 1586, 1389, 1116, 941, 789 and 634, respectively.
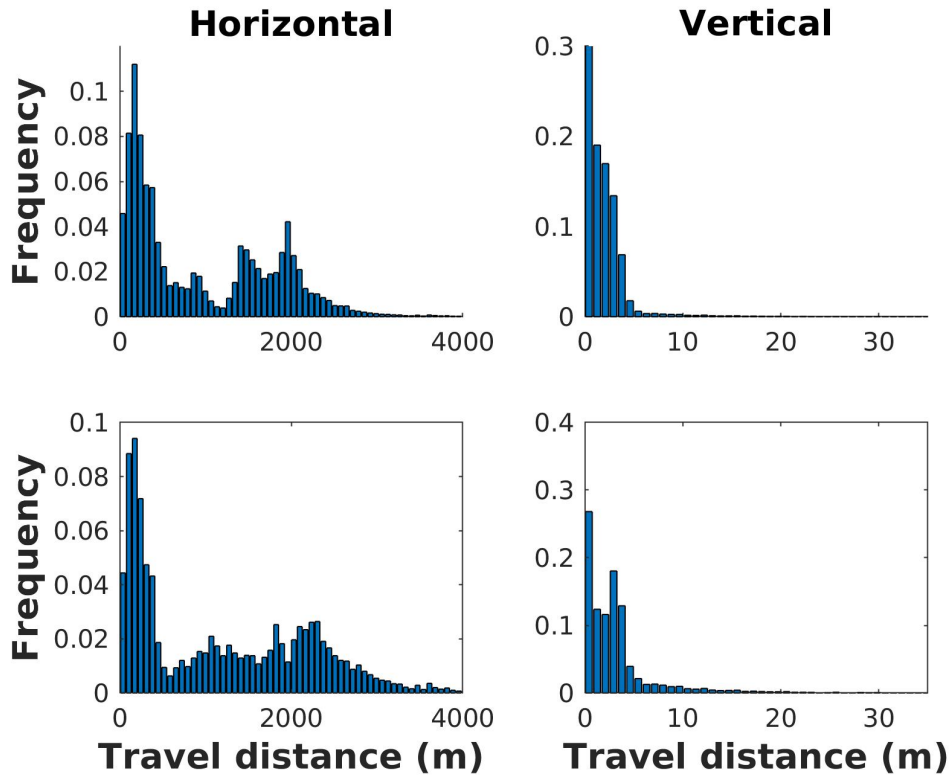
Figure 16. Histograms of horizontal (left panels) and vertical (right panels) transport distance of particles within Red square (upper panels) and white rectangular (lower panels) in Figure 2. The calculation of distance is between the location of the last snapshot at T = 27.5 hours and the initial location.
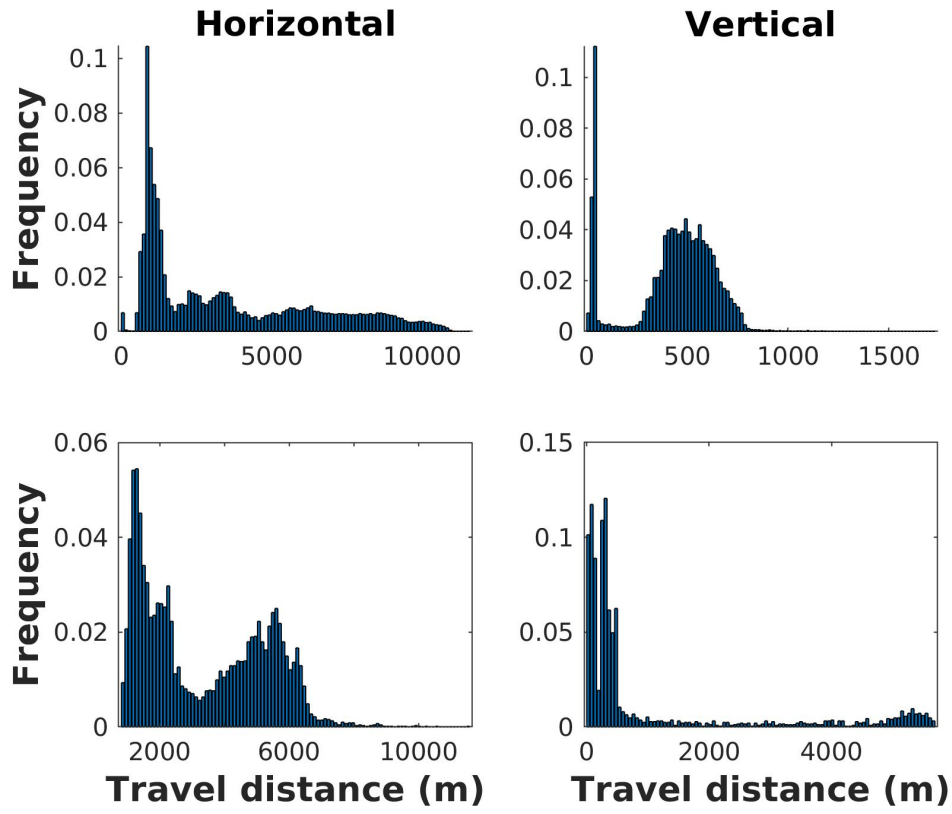
709 **Figure 17.** Same with Figure 16 but with particle transport distance integrated over time.